Exploiting Total Internal Reflection Geometry for Terahertz Devices and Enhanced Sample Characterization

Qiushuo Sun[#], Xuequan Chen[#], Xudong Liu, Rayko I. Stantchev, Emma Pickwell-MacPherson[*]

Q. Sun, Dr. X. Chen, Dr. R. I. Stantchev, Prof. E. Pickwell-MacPherson
Department of Electronic Engineering, The Chinese University of Hong Kong, Hong Kong
Shatin, N.T., Hong Kong, 999077, China
Dr. X. Liu
National-Regional Key Technology Engineering Laboratory for Medical Ultrasound, Guangdong Key Laboratory for Biomedical Measurements and Ultrasound Imaging, Department of Biomedical Engineering, School of Medicine, Shenzhen University
Shenzhen, 518060, China
Prof. E. Pickwell-MacPherson
Physics Department, University of Warwick, Coventry, CV4 7AL, United Kingdom
E-mail: E.MacPherson@warwick.ac.uk
#These authors contributed equally to this work.

Abstract: To promote potential applications of terahertz (THz) technology more advanced functional THz devices with high performance are needed, including modulators, polarizers, lenses, wave retarders and anti-reflection coatings. This article summarizes recent progress in THz components built on functional materials including graphene, vanadium dioxide and metamaterials. Our key message is that while the choice of materials used in such devices is important, the geometry in which they are employed also has a significant effect on the performance achieved. In particular, we review devices operating in total internal reflection geometry and explain how this geometry is able to be exploited to achieve a variety of THz devices with broadband operation.

Keywords: Terahertz, Total internal reflection, modulators, polarization, graphene, metamaterial

1. Introduction

Terahertz (THz) radiation has received increasing interest from research groups around the world due to its potential applications in material characterization, security checking, communication

engineering, automotive engineering, biomedical engineering and heritage screening[1]. THz time domain spectroscopy (THz TDS) has been proposed[2] and applied to study a wide range of materials, including semiconductors[3], ceramics[4], aqueous solutions[5] and organic materials[6]. The resonant frequencies of some intermolecular bonds are located in the THz frequency range[7] which helps analyze the dynamic vibrations in the materials[8]. The non-ionizing nature of THz light (4.14 meV at 1 THz) and low power (around 100 μW) characteristics of the commercially available systems, make THz imaging suitable even for *in vivo* measurements[9].

Emission and detection in time-domain THz systems can be achieved by a variety of laser-driven devices, some of which will be mentioned here. Photoconductive antennas can emit and detect THz light with a femtosecond pumping laser centered at the wavelength of either 800 nm or 1550 nm[10]. Non-linear optical rectification and air-plasma approaches radiate a broader spectrum up to the mid-infrared[11], and the inverse application of optical rectification enables an electro-optic sampling technique which also supports a broader detection bandwidth[12]. Frequency-domain techniques have also found important roles in the THz regime. For example, backward wave oscillators with frequency-tuning ability and milliwatt output power enable imaging and spectroscopy with a higher signal-to-noise ratio (SNR) and better tolerance on the insertion loss[13]. Heterodyne detectors able to resolve the absorption lines such as that of liquid H_2O[14] have excellent spectral resolution and are key for atmospheric detection of molecules. Homodyne transceivers have been successfully employed in large field-of-view imaging for security[15], and field-effect transistors provide another option to make on-chip array detectors for imaging[16]. Functional devices such as modulators, polarizers, waveguides, lenses and antireflection coatings, with high performances for this frequency range are needed to support all the potential imaging modalities and applications. However there is still a lack of affordable and effective THz components.

In this progress report, we discuss recent advances in THz functional components and material characterization techniques, and in particular highlight the progress in devices exploiting total internal reflection (TIR) geometry. In 2016 Liu *et al* employed TIR geometry to improve the design of a THz spatial light modulator[17]. By using TIR instead of transmission geometry much smaller changes in the conductivity of the modulation substrate are needed to obtain a high modulation depth. This has many implications as it is significantly easier to change the conductivity of materials by smaller amounts, for example graphene, by ~9 mS in TIR compared to ~60 mS in transmission. Liu *et al* derived the theory to explain this phenomenon and demonstrated high performance THz modulators fabricated from photoexcited silicon[17a] and electrically gated graphene[17b]. It should be noted that although the structure of the TIR modulator is similar to the Kretschmann configuration of traditional surface plasmons designs, the mechanism is totally different. In the TIR modulator, the conductive layer attenuates the broadband incident THz signal rather exciting surface plasmons in a resonant manner; and thus shows a broadband response for both s- and p- polarizations. This work has therefore opened up an avenue of research and inspired other broadband THz devices and techniques to be designed using TIR geometry including polarization control devices and a highly sensitive method for characterizing conductive thin film materials. Six of our TIR devices are illustrated in **Figure 1**. Noting the sensitivity of devices to the angle of incidence has also led to the design of a graphene/quartz device operating at the Brewster angle for high performance THz amplitude and phase modulation[18].

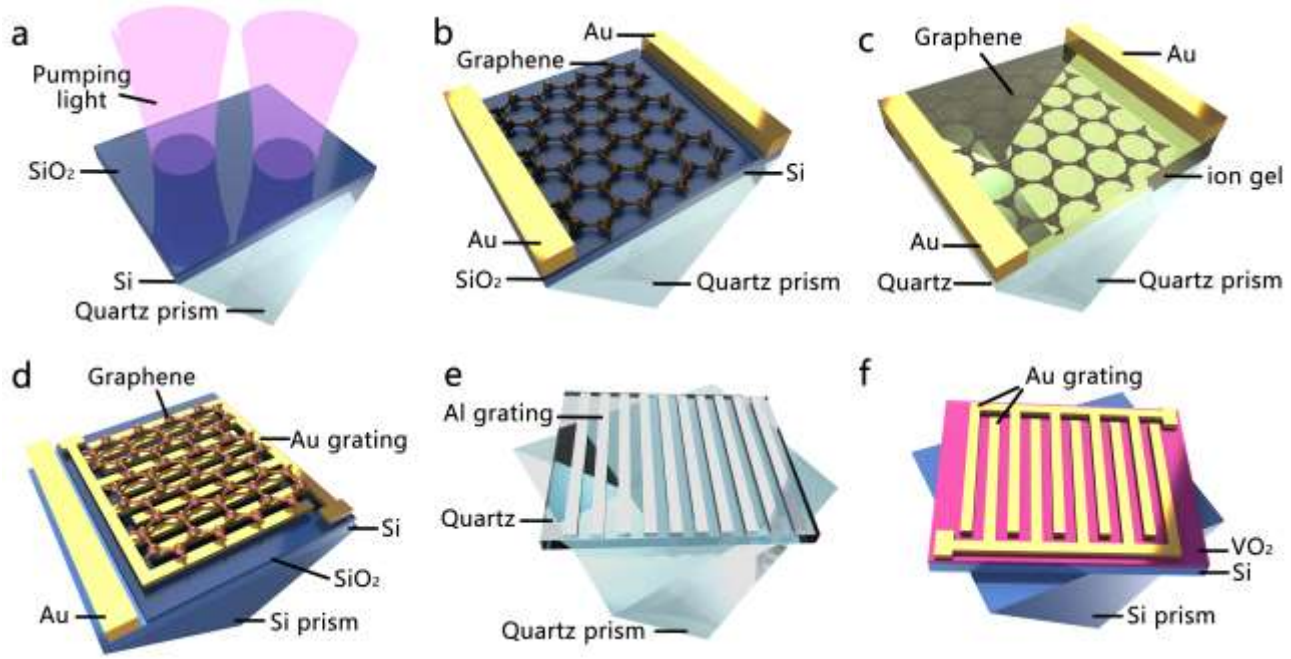

Figure 1. (a) Optically controlled spatial light modulator, (b) Electrically controlled graphene based modulator, (c) Electrically controlled graphene with ion gel based modulator, (d) Electrically controlled graphene loaded grating high speed modulator (e) Polarisation converter (passive control), (f) Polarization converter with active control.

In this article, we explain our rationale for the designs of the various devices presented, and we also aim to clarify any misconceptions that readers may have had due to the fundamental physics being different from perhaps what they were expecting. In section 2.1 we introduce the key concepts of the TIR approach and then summarize the main features and capabilities of the devices we have developed building on this phenomenon in sections 2.2-2.5, namely an optically controlled silicon based modulator, and electrically controlled graphene modulators, passive and active polarization converters, and a sensor for thin film characterisation. In section 3 we show how the TIR modulator design can be utilised to achieve rapid single pixel THz imaging. In section 4, continuing the theme of exploiting incident angle dependent phenomena, we show how the Brewster angle can be exploited to achieve rapid, deep and broadband phase and amplitude modulation. In section 5 we review the challenges still needing to be addressed and emphasize how careful consideration of the geometry of

materials can facilitate development of more high-performance THz devices in the future.

2. Utilization of TIR geometry in THz devices

2.1 TIR for THz devices

One of the key devices lacking in the THz community is a THz spatial light modulator. An ideal THz modulator will be able to modulate broadband THz light with high speed and modulation depth (MD), and should also be easily scalable for large area spatial modulation. So as to be able to build on existing digital micromirror device (DMD) technology used at optical frequencies, optical modulation of semiconductors and metamaterials is commonly used to modulate THz light[19]. When a semiconductor receives energy higher than its band gap, free carriers are generated, and the conductivity of the material is altered depending on the recombination time, carrier density and diffusion length of these carriers. By tuning the power and wavelength of the pumping light, the desired changes in conductivity of the semiconductor can be controlled. Organic semiconductor thin films[20] and two dimensional materials such as MoS_2[21], WSe_2[22], and graphene[23] coated on silicon substrate can realize high modulator depths when laser light is pumped onto them. Some optically modulated devices utilize metamaterial structures to enhance the light-matter interaction[21]. The conductivity of materials can also be controlled electrically by electric injection and depletion of charge carriers[19]: a 5 x 5 cm^2 spatial light modulator built on electrically tuned graphene supercapacitors achieved a MD from 40-60% at 0.1-1.5 THz[24]. Thermal modulators[25], magnetic modulators[26] and other non-linear modulators[27] have also shown promising performance. However, it is still challenging to make a modulator that satisfies all the requirements, including high MD, quick response, simple fabrication process and broad operational bandwidth. In the next sections, we present THz devices based on silicon, graphene and vanadium dioxide (VO_2) that are either operated

electrically or optically, combined with total internal reflection (TIR) regime or metamaterial structures to accomplish high performance. In this section we will focus on the fundamental underlying theory.

Transmission geometry is commonly used in most THz modulators that are controlled by conductive thin film attenuation. However, the attenuation caused by the sample in transmission is relatively low, the short interaction length constrains the MD of the device. Consequently, reflection spectroscopy is considered. In reflection geometry, the reflection coefficient *r* from a three-layer structure (medium 1 – conductive thin film - medium 2) can be written by Equation (1.1) (for s-polarization); Similar to the transmission, the amplitude of the reflected THz light depends on the sheet conductivity σ_s [17a], while the mechanism is different. Unlike transmission, the conductive film directly reflects and absorbs the light; the mechanism of reflection is not that straightforward and can be explained by different theories. The equivalent circuit model can be used to show that when the conductivity of the thin conductive film reaches an impedance matching condition to the system, a zero reflection can be achieved[28]. Such concept has been applied to design various anti-reflection coatings[29]. Interference theory provides a simpler view to the role of the conductive thin film. When the conductivity becomes zero in Equation (1.1), the equation returns back to a standard Fresnel equation resulting in a reflection phase close to zero when $n_{m1}>n_{m2}$. When the conductivity is sufficiently large so that the Fresnel terms can be ignored, the reflection becomes metallic with a 180□ phase change. Therefore, a very small reflection can be achieved at the interference of these two out-of-phase reflections by carefully tuning the conductivity.

$$r = \frac{n_{m1}\cos\theta_{m1} - n_{m2}\cos\theta_{m2} - Z_0\sigma_s}{n_{m1}\cos\theta_{m1} + n_{m2}\cos\theta_{m2} + Z_0\sigma_s} \tag{1.1}$$

To avoid large insertion losses, ordinary reflection geometry can be replaced by TIR geometry[17a], in which the signal is totally reflected from the sample interface, as illustrated in **Figure 2(a)**.

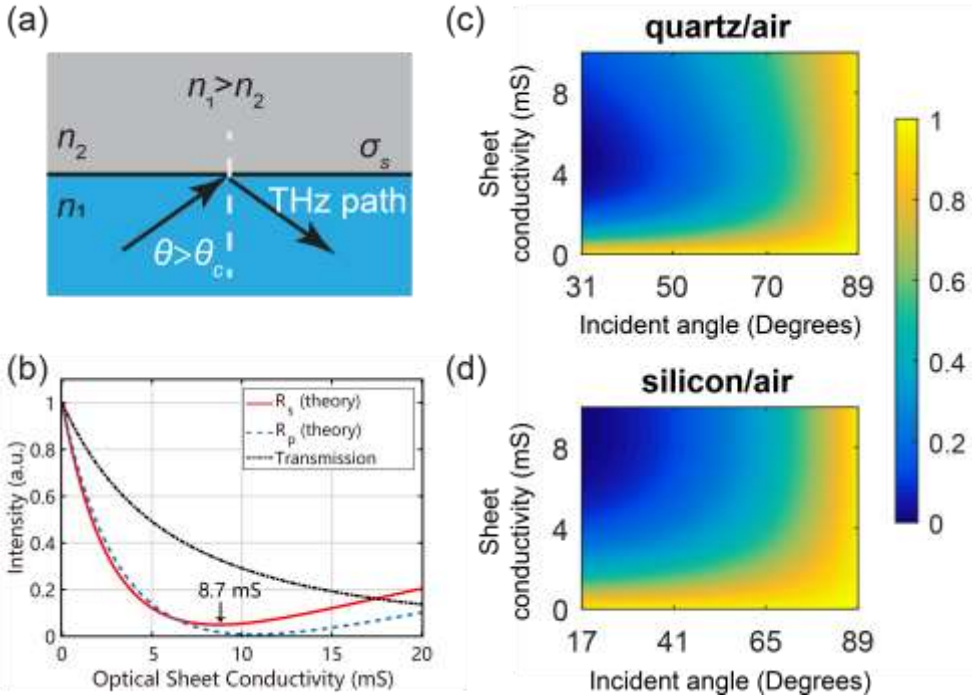

Figure. 2 (a) Schematic of the TIR geometry. (b) Calculated and simulated relative intensity of the reflected/transmitted signals as a function of optical sheet conductivity[17a]. Reflected intensity based on various material combinations and sheet conductivity in s-polarization, (c) quartz-air and (d) silicon-air. The sheet conductivity changes from 0 to 10 mS. The incident angle varies from critical angle to grazing incidence.

To compare the sensitivity between two geometries, the relative intensity changes in transmission coefficient t and reflection coefficient r under a 24.6□ incident angle are given in Figure 2(b) as a function of sheet conductivity σ_s. For a given increase in the optical sheet conductivity, the relative intensity of the reflected signal in the TIR regime has a more significant drop compared to that of the transmitted signal. When the sheet conductivity is 8.7 mS, the reflected signal R_s reaches zero whilst it needs to reach 62 mS for the transmitted signal. Consequently, a THz modulator built in TIR geometry can achieve a higher MD for a certain change in the sheet conductivity. The key equations to calculate the reflection coefficient for *s*- and *p*- polarization light with conductive interface in the TIR regime are given below[17b]:

$$r_s = \frac{n_1 \cos\theta_i - i \cdot \sqrt{n_1^2 \sin^2\theta_i - n_2^2} - Z_0\sigma_s}{n_1 \cos\theta_i + i \cdot \sqrt{n_1^2 \sin^2\theta_i - n_2^2} + Z_0\sigma_s} \tag{1.2}$$

$$r_p = \frac{i \cdot n_1\sqrt{n_1^2 \sin^2\theta_i - n_2^2} - n_2^2 \cos\theta_i - i \cdot Z_0\sigma_s \cos\theta_i \sqrt{n_1^2 \sin^2\theta_i - n_2^2}}{i \cdot n_1\sqrt{n_1^2 \sin^2\theta_i - n_2^2} + n_2^2 \cos\theta_i + i \cdot Z_0\sigma_s \cos\theta_i \sqrt{n_1^2 \sin^2\theta_i - n_2^2}} \tag{1.3}$$

where n_1 is the refractive index of the incident side medium, n_2 is the refractive index of the refraction side medium, θ_i is the supercritical incident angle, Z_0 is the vacuum impedance (377 Ω) and σ_s is the optical sheet conductivity. The reflection coefficients clearly depend on the fundamental material properties of the substrate and upper medium as well as the incident angle, as shown in Figure 2(c-d). Therefore the choice of materials can be tailored to the desired physical system, e.g. a less than 0.5% reflected intensity can be achieved in a quartz/TOPAS design at the incident angle of 51° with the lowest conductivity of 3.4 mS[17b].

2.2 Optically controlled silicon TIR modulator

To develop a device that can be optically modulated, as shown in **Figure 3(a)**, a silicon substrate was placed on top of a quartz prism with the refractive angle being 24.6° [17a] (this is larger than the critical angle between silicon and air). The sheet conductivity of the silicon was altered by pumping a 450 nm light from a diode laser. Figure 3 (b) gives the THz spectra of the measured MD in two geometries with various pumping powers, where the MD was calculated by $MD=(1-I_p(\omega)/I_0(\omega))*100\%$, I_p and I_0 are the intensity of the transmitted or reflected THz signal with and without pump, respectively. Impressively, the MD in reflection geometry with 280 mW/cm^2 pumping power was already higher than the MD in transmission with 775 mW/cm^2. The highest MD that the reflection geometry could reach was close to 100% between 0.2-0.7 THz, whilst the highest MD in transmission geometry was less than 80%. With having proved the high performance of the proposed device, a cheap light source (LED, 450 nm, 475 mW/cm^2) instead of a laser was applied to realize the spatial THz modulation,

the reflected intensity images are given in Figure 3 (c-d).

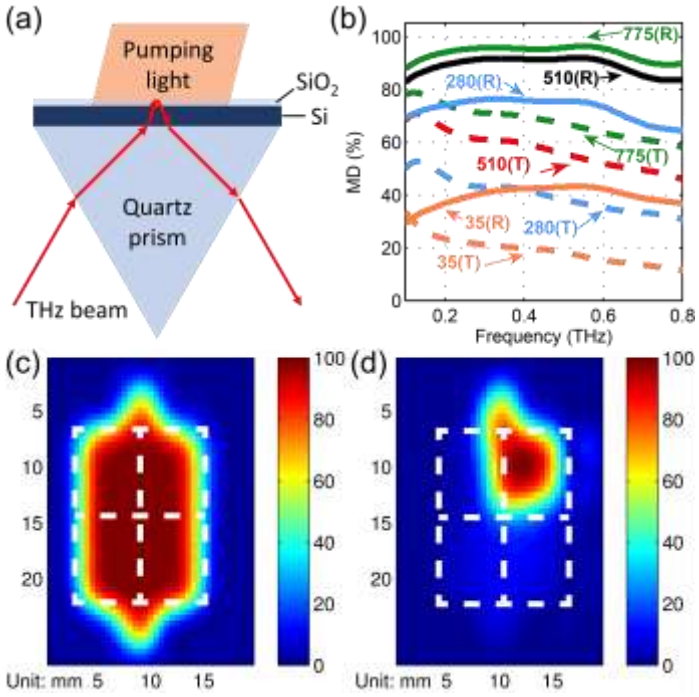

Figure 3. (a) Schematic diagram of the silicon on quartz prism device in TIR geometry, (b) Measured MD of the device with various pumping powers in TIR (R) and transmission geometries (T), (c) and (d) THz intensity images at 0.5 THz when the pumping light is off and on within ¾ of the area [17a].

When there was no pumping light, the signal reflected from the prism surface area had uniform and high intensity, but when ¾ of the area was exposed to the LED light and ¼ of the area was in dark, a high contrast between the areas was observed from the THz image. The MD at the pumped area was as high as 99.9% resulting in the reflected THz signal effectively being blocked out. This work proved that TIR helps increase the MD depth significantly compared to transmission geometry, and that an extremely high MD can be reached by an LED source, a silicon substrate and a quartz prism. This approach therefore provides a low cost and scalable solution to broadband THz light modulation, and can be easily adopted with a DMD to realize fast and flexible spatial modulation up to 20 kHz (the switch rate limit of DMDs). This will be demonstrated in section 3.

2.3 Electrically controlled graphene TIR modulators

Graphene has some exceptional properties compared to other semiconducting materials. In particular

its high electron mobility makes it a favorable material to build modulators and other functional devices with broadband performance and high modulation speed[30]. The conductivity of graphene can be manipulated easily from high-resistance state to semi-metal state by applying a gate voltage[18]. Consequently, building on the optical device in section 2.2, we designed an electrical device by putting a graphene field-effect transistor on top a quartz prism. The graphene conductivity was tuned between 0.94 mS and 2.1 mS by applying the gate voltage in the range of -9 to +15 V[17b]. The experimental setup is given in **Figure 4**(a), the voltage was applied between the contact electrode and the gate electrodes on the side. The measured time domain pulses reflected from the graphene device in the TIR regime with various voltages are shown in Figure 4(b). The highest MD in the frequency domain was 15% in transmission geometry, compared to 40% in TIR (Figure 4(c)).

To achieve a wider range of graphene conductivity we modified the device in Figure 4(a) to have ion-gel gated graphene. This increased the conductivity range to 0.5-5.1 mS with a lower gating voltage of -0.1 V to 2 V. To increase the MD further, the medium under the graphene layer was also changed from silicon to quartz, as shown in Figure 4(d). Theoretically, when the sheet conductivity is less than 4.7 mS, the quartz setup has a higher modulation sensitivity to the sheet conductivity.

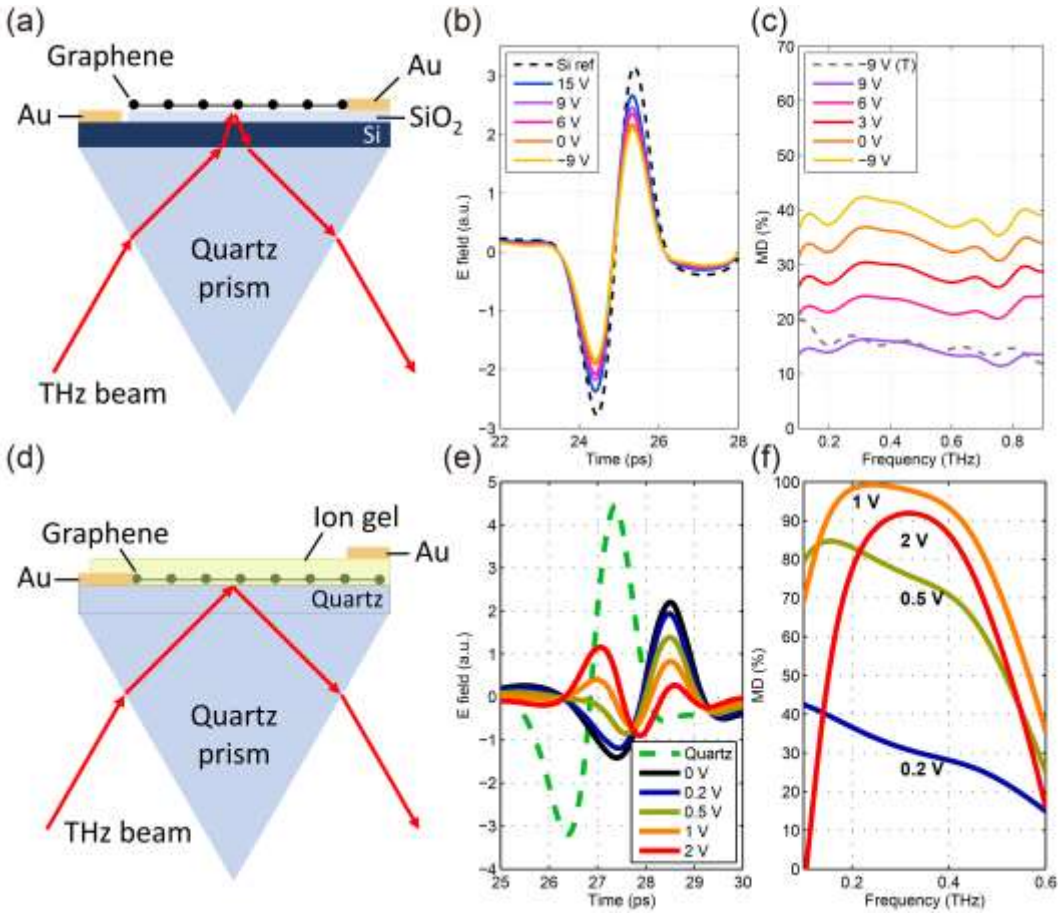

Figure 4. Schematic diagrams of the graphene device (a) without and (d) with ion-gel in the TIR geometry; Reflected time domain waveforms for from the TIR-graphene device (b) without and (e) with ion-gel under different gate voltages in s-polarization; The corresponding MD of the TIR-graphene device under different gate voltages (c) without and (f) with ion-gel in the frequency-domain. In (c) the MD was defined relative to the 15 V measurement and the corresponding maximum MD in transmission is shown (dashed gray line) for comparison[17b]. In (f) the MD was defined relative to the 0 V measurement.

From Figure 4(e) and 4(f), we can see that from 0 V to 1 V, the peak to peak of the THz pulse decreased rapidly and reached the maximum MD of 99.3%[17b]. The results here outperform a similar device reported by Harada et al.[31] in the same year: their device was a passive device with an attenuation of ~70%. As shown in Figure 4(e), the time domain signal at 2 V shows reversed phase compared with the signal at 0 V. This feature inspired us to tune the sheet conductivity to be at the point where the phase changes abruptly to achieve a sensitive phase modulator. The iongel devices achieved deep modulation, but their stability and operation speed are not good enough for practical

applications[32] and this motivated our next idea.

To maintain the deep modulation while using a solid-state device, instead of using iongel, we proposed a metal wire grating integrated graphene device. Metal wire gratings have a non-resonant electric field enhancement effect, which can enhance the electric field in a broadband frequency range with an enhancement factor being *P/w* (where *P* and *w* are the period and gap width of the subwavelength grating)[33]. Combining this enhancement effect with the evanescent wave in the TIR geometry can lead to a deep modulation. We have derive theoretical equations based on Equation 1.3 to describe the behavior of the grating structure . The new equation for s- polarized light is given below:

$$r_s = \frac{n_1 \cos\theta_i - i \cdot \sqrt{n_1^2 \sin^2\theta_i - n_2^2} - \eta \cdot Z_0 \sigma_s}{n_1 \cos\theta_i + i \cdot \sqrt{n_1^2 \sin^2\theta_i - n_2^2} + \eta \cdot Z_0 \sigma_s} \tag{1.4}$$

where η is the enhancement factor, $\eta = P/w$. Compared to Equation 1.3, Equation 1.4 has an enhancement factor before the sheet conductivity part. It indicates we can achieve the same modulation depth but only with $1/\eta$ of the original sheet conductivity. Considering the case of air/Si (**Figure 5(b)),** the required sheet conductivity for a high attenuation can be lowered from ~9 mS to only 0.9 mS (with η=10). Shi et al. achieved a MD of approximately 84% [34] with a metal wire grating in transmission geometry, but still used ion-gel gated graphene. We fabricated metal wire grating integrated SiO_2/Si gated graphene devices (period: 30 μm, gap: 15 μm and period: 30 μm, gap: 10 μm) and measured them using a a THz-TDS system in TIR geometry as shown in Figure 5(a)[35]. A graphene layer (size: 1 cm× 0.5 cm) was transferred onto the metal grating area (size: 0.5 cm× 0.5 cm).

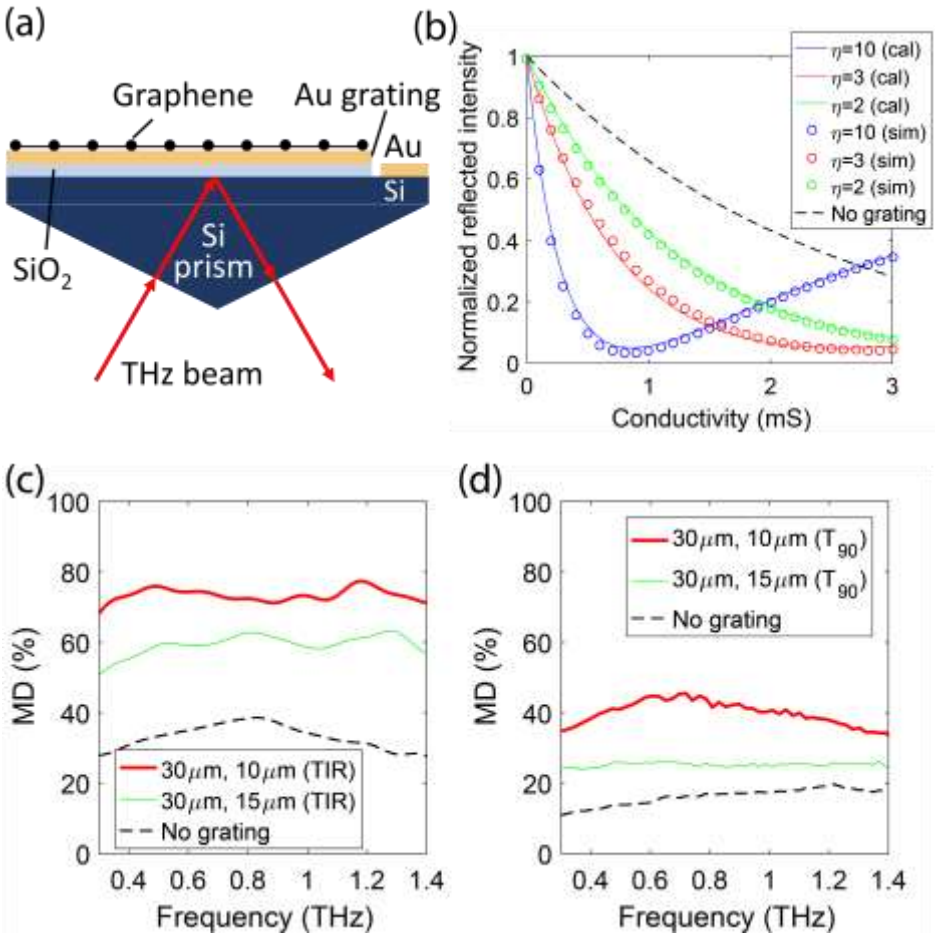

Figure 5. (a) Schematic of the graphene-loaded metal wire grating modulator in the TIR geometry. The graphene device was deposited on high-resistivity SiO2/Si substrate and placed on a Si prism. The conductivity of graphene was adjusted by the voltage between the Si substrate and metal grating. The incident THz signal was in s-polarization. (b) Simulation and calculation results of the reflected intensity from the graphene/metal grating. The solid lines are calculation results and the dots are simulation results with different enhancement factors (η). The black dashed lines are the calculation results without a metal grating. (c) and (d) are the MDs of the two devices in the TIR and in transmission geometry (T90). The red solid line is the MD of graphene integrated with a 30 μm period and a 10 μm gap (30 μm ,10 μm) grating; the blue solid line is the MD of graphene integrated with 30 μm period and a 15 μm gap (30 μm,15 μm) grating; the black dashed line is the MD of graphene without a metal grating.

The bare graphene area was used to make a comparison with the metal grating integrated area. An average MD of ~77% was achieved across the range of 0.2-1.4 THz with the 30 μm, 10 μm device, nicely matching our theory. The MD was 4.5 times higher than that of the device without a metal grating in transmission geometry. A higher enhancement factor device (P=20 μm, g= 2μm, η=10) could be fabricated to achieve even higher MD. However, the fabrication difficulty when the gap width goes to submicron levels will be higher, while increasing the period may lead to a lower cut-

off frequency. Nevertheless, since no ion gel was used, this device could be switched more robustly with a potential higher operation speed. These results therefore provide the fundamental demonstration of a device which can be rapidly and robustly switched with a high MD and offers a potential solution for single-pixel imaging.

2.4 Polarization converters in the TIR regime

Polarization is a basic and important physical property of electromagnetic waves. Any polarization-dependent light-material interaction requires proper control of the polarization state. Polarization manipulation primarily includes linear polarization filtering, quarter-wave and half-wave retardance. The common foundation of these manipulations is that they are all based on modulation of the amplitude and phase for one or more polarization components. For example, filtering out a linear component by a polarizer is realized by eliminating the amplitude in the blocking direction with very little decay to the passed component. Quarter-wave or half-wave plates provide an extra 90□ or 180□ phase delay to one component compared to its orthogonal component. Therefore, efficiently and accurately modulating the amplitude and phase is essential to realize good polarization control. Various techniques have been introduced in the THz range. For example, metallic gratings have been widely used for polarizers[36], liquid crystals are capable of quarter-wave conversion[37], and metamaterials are flexible in pattern designs to realize different types of polarization output[38]. Compared to the optical region, most of these devices are still away from perfection and they have limitations in different aspects. The most mature devices are commercially available THz polarizers; they have good performance for the extinction ratio, operation bandwidth, insertion loss and robustness. However, quarter-wave and half-wave converters are a lot more challenging as both the amplitude and phase need to be modulated, and the state-of-art devices still suffer from either the accuracy, active control, operation bandwidth or modulation speed. A common approach at visible

frequencies is to use liquid crystal-based phase shifters. The birefringence provides a different phase delay but similar transmission to the two orthogonal E-field components. The biggest issue when applying liquid crystals in the THz range is the orders of magnitude lower switching speed from milliseconds to minutes due to the wavelength-comparable cell thickness[37c, 39]. Metamaterials are also popular candidates, but they usually operate in a narrow band[38c, 40].

2.4.1. Passive polarization control

In addition to the amplitude modulators described earlier, our TIR based approach can also be applied to develop polarization control devices. Our TIR-grating structure is able to function as both quarter-wave and half-wave conversion in a broadband manner[38b].

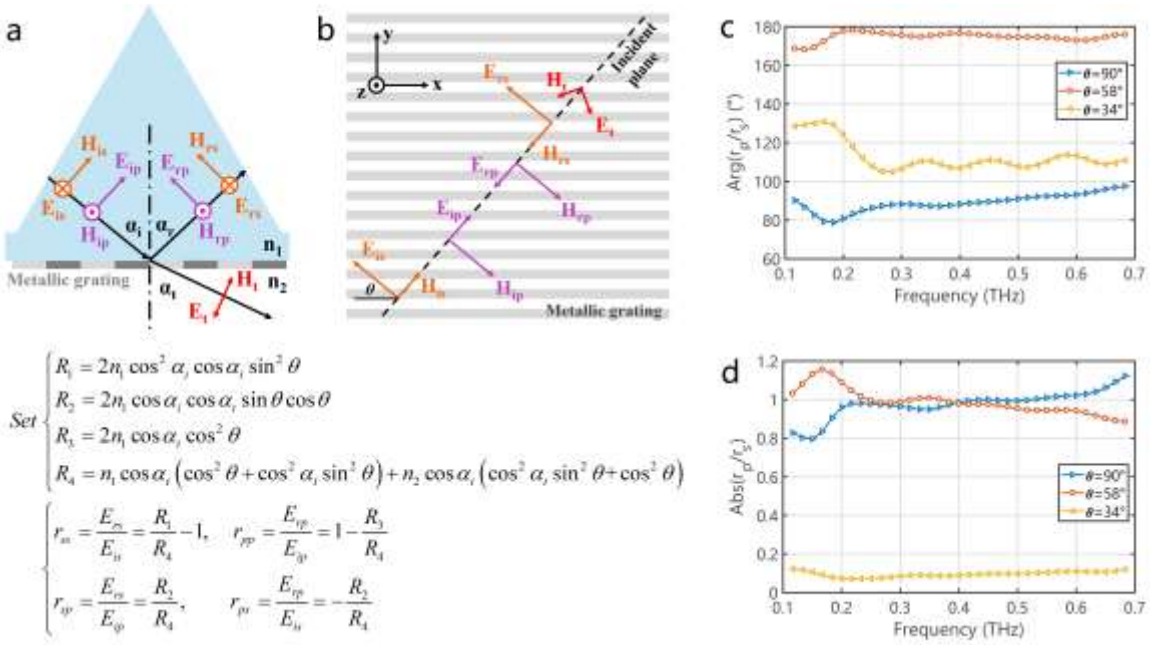

Figure 6. **(a)** THz light interaction with the grating from the incident-plane view. **(b)** Top view of the E-H fields of the incident, reflected and transmitted components. **(c)** Magnitude ratio and **(d)** phase difference between the p- and s- components when θ=90□, 58□ and 34□ respectively, corresponding to a quarter-wave conversion, half-wave conversion and 45□ linear rotation.

As shown in **Figure 6(a)**, the device employed a quartz prism coupled with a quartz plate with metallic grating on the bottom surface. The lower plate could be freely rotated to change the grating

orientation. The reflection theory from the anisotropic grating interface was derived to show how the device is able to achieve multifunctional polarization control. For example, at the incident angle of 52□, illuminating a 45□ (to the p-component) polarized light to the device, a 45□ linear rotation, a half-wave conversion and a quarter-wave conversion were achieved when the grating orientation was at 34□, 58.5□ and 90□ respectively. The magnitude ratios and phase differences between the p- and s-components at these three θ values are given in Figure 6(c) and (d) respectively. When θ=90□ and 58□, the magnitude ratios were both close to 1 while the phase differences are close to 90□ and 180□ respectively. These indicate the reflected beam became circularly and 90□ linear rotated at these two grating orientations. Further rotating the grating to θ=34□ gives a magnitude ratio close to zero, which means the s-polarized light was reflected and it was 45□ linear rotated compared to the incident light. All the three states showed very small dispersion in the frequency range from 0.1 THz to 0.7 THz. Therefore, three different polarization manipulations were realized in a broadband manner by a single device. The key equations we derived to explain this phenomenon are given below Figure 6(a) and (b). The cosθ and sinθ terms can efficiently change the reflection coefficients of the s- and p-components, and thus result in various polarization states. A video demonstrating the phenomenon and how we discovered it by simply rotating a wire grid polarizer on a quartz prism, is available at this link[41].

2.4.2. Active polarization control

To advance this further, VO_2, a phase-transition material which can be electrically and thermally controlled, was employed to enable active electrical control[38f]. The VO_2 layer was sandwiched in-between the silicon substrate and the gold grating. The grating also acted as electrodes to switch the phase of the VO_2. When the VO_2 was in the insulating phase, the nanometre thickness made it

transparent to the THz light and the device followed the reflection theory derived from the previous work[38b]. The output polarization can be controlled by rotating the grating orientation. By applying a bias voltage to switch the VO_2 to its metallic phase, a semi-metallic reflection was generated in the periodic direction of the grating. The device coupled with a Si prism is illustrated in **Figure 7(a)**. An important functionality enabled by introducing the VO_2 layer is the active linear-circular polarization switching.

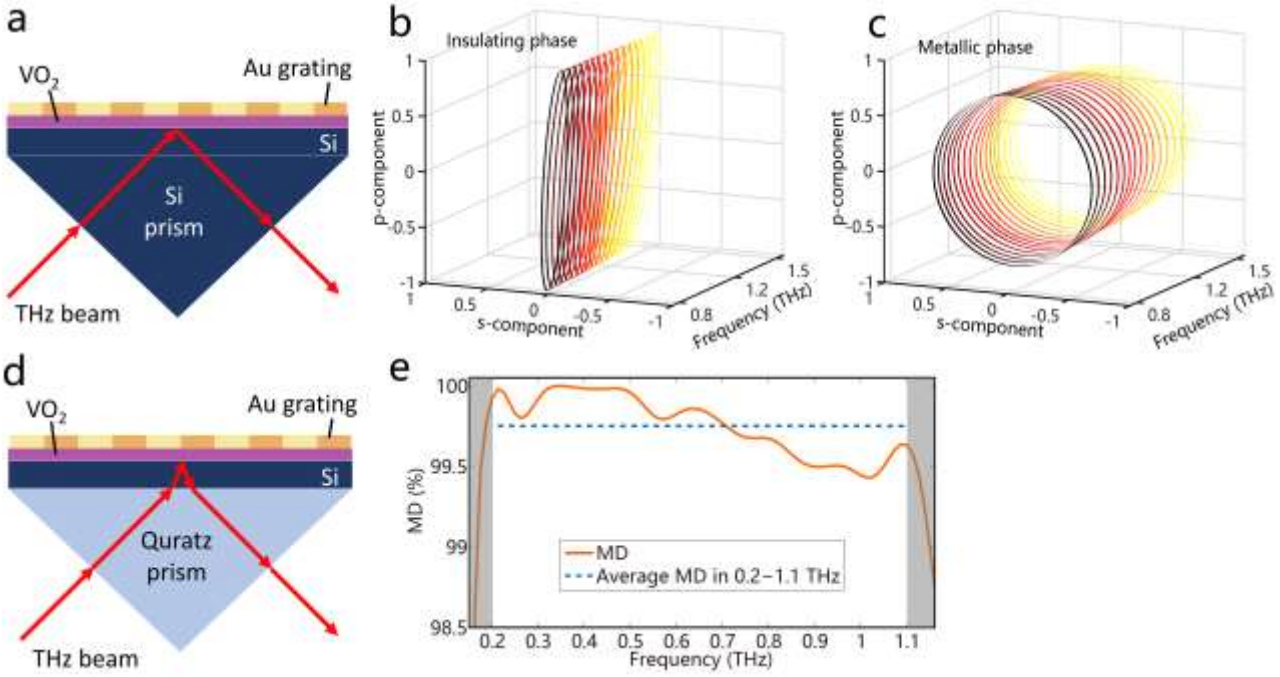

Figure 7. (a) Diagram of the TIR-VO_2-grating multifunctional polarizer controlling device. (b) Linear-circular polarization switch by the proposed TIR-VO_2-grating device. p-polarized linear output when the VO_2 was at the insulating phase. (c) Circular polarization output when the VO_2 was at the metallic phase. (d) Diagram of the same TIR-VO_2-grating device coupled with a quartz prism. (e) Modulation depth as a function of frequency. The white area shows the effective region and the gray areas have low SNR.

As shown in Figure 7 (b), at an incident angle of 45□ and in the insulating state of the VO_2, the device still follows the previously derived equations due to the ignorable conductivity of the VO_2. P-polarized light was reflected by rotating the incident light by 45□, which matches well with the theoretical calculation. The polarization states were still frequency-independent. Electrically

switching the VO_2 to the metallic phase produced circular polarizations from 0.8 THz to 1.5 THz with a very small dispersion, as shown in Figure 7(c). A linear-circular polarization switch was thus realized by active electrical control. Of course, the proposed device is still not perfect in every aspect. The major limits come from the slow switching speed of the VO_2 and the need for properly designing the VO_2 thickness. In the THz range, polarization manipulation devices still need to be further improved in terms of speed, accuracy and operation bandwidth. For example, searching for faster and more efficient active materials may support more accurate and stable polarization control, better structural designs may provide broader operation bandwidth to metamaterial devices or faster switching speed for liquid crystal elements. The development of these devices will be relevant to applications in THz spectroscopy, communications and imaging.

The device can also function as an intensity modulator by replacing the silicon prism with a quartz prism to introduce a 24.5□ incident angle to the Si-VO_2-grating interface, as shown in Figure 7(d). By illuminating with s-polarized light and setting the grating at θ=47.5□, the device functioned as a half-wave converter to give a p-polarized reflection when the VO_2 was in the insulating phase. Switching the VO_2 to its metallic phase strongly enhanced the s-reflection and provided an average MD of 99.75% from 0.2 THz to 1.1 THz in the s-direction, as shown in the white region of Figure 7(e). The high modulation efficiency was due to the huge conductivity change of the VO_2[42], which can be further improved by increasing the layer thickness. Although the modulation can be easily controlled by an electrical bias, the intrinsic physics of the phase transition is based on temperature variation. This obviously limits the switching speed especially for the cooling process. Furthermore, the high temperature sensitivity also makes it difficult to gradually vary the conductivity between the metallic and insulating phase, which results in another disadvantage that it usually only works in a ON-OFF binary mode. Therefore, semiconducting devices such as graphene are usually more

favourable for modulators as they can be precisely controlled and support a modulation rate up to megahertz. Therefore, VO_2 enabled active devices may find applications that requires a binary and slow switch.

2.5 The TIR regime and multilayer structures for material sensing

Employing suitable geometries for material characterization is important as different geometries provide different sensitivities. For example, transmission gives the best contrast for most transparent materials[43], attenuated total internal reflection (ATR) provides higher sensitivity for highly absorptive liquids[44], whilst ellipsometry is good for opaque solids[45]. Specially designed structures have also been reported to enhance the characterization sensitivity. For example the Fabry-Perot effect is used for frequency-domain THz ellipsometry, which has been successfully applied to measure metallic oxide[46], gas[13b] and the Hall effect[47]. Here, we show how the TIR geometry can be used as a sensor to enhance the contrast of thin-film samples.

Perovskites are novel materials for photovoltaic solar cells (PSCs)[48], LEDs[49] and lasers[50]. Particularly, PSCs have reached an efficiency higher than 22%. One issue that stops the PSCs from real application is their low stability, for example, moisture, oxygen, light and heat can all cause degradation of methylammonium (MA) lead halide perovskites[51]. Understanding the interaction between the light and the crystal structure of the perovskites is essential to improve the stability and efficiency of PSCs. When the illumination energy is higher than the bandgap of the perovskites, the structural and electronic properties of the material might be modified. For MA perovskites, it has been shown that the binding energy between the MA cations and the inorganic octahedra decreases, causing an increased rotational freedom of the MA cations, which consequently induces changes in the octahedra[52]. THz time resolved spectroscopy can capture the carrier dynamics at the picosecond-

nanosecond level, and the recombination rate constants and diffusion length can be extracted[53]. However, the photo-induced degradation happens on a much slower time scale, THz time domain transmission spectroscopy is potentially suitable for monitoring this as it can detect the changes in the low-frequency vibrational modes, which are related to electron-phonon scattering rate and mobility. However, there is less than a 10% change in the intensity of the transmitted light from a 300 nm thick $MAPbI_3$ film[8] and this is difficult to detect in the usual geometry of THz time domain transmission spectroscopy.

As calculated in Figure 1(b), in TIR geometry, there is a more significant change in the reflected signal intensity when the conductivity of the optical sheet changes compared to the transmitted signal. Therefore to measure photo-induced structural changes in the perovskite thin films, we used THz time domain spectroscopy TIR geometry instead of transmission geometry. **Figure 8 (a)** shows the schematic of the setup: a quartz prism was used to satisfy the conditions of TIR, and the perovskite thin film was spin coated onto the quartz substrate. The spectra of four perovskite samples, $MAPbI_3$, $MAPbI_{2.5}Br_{0.5}$, $MAPbI_2Br_1$ and $MAPbBr_3$, are illustrated in Figure 8 (b).

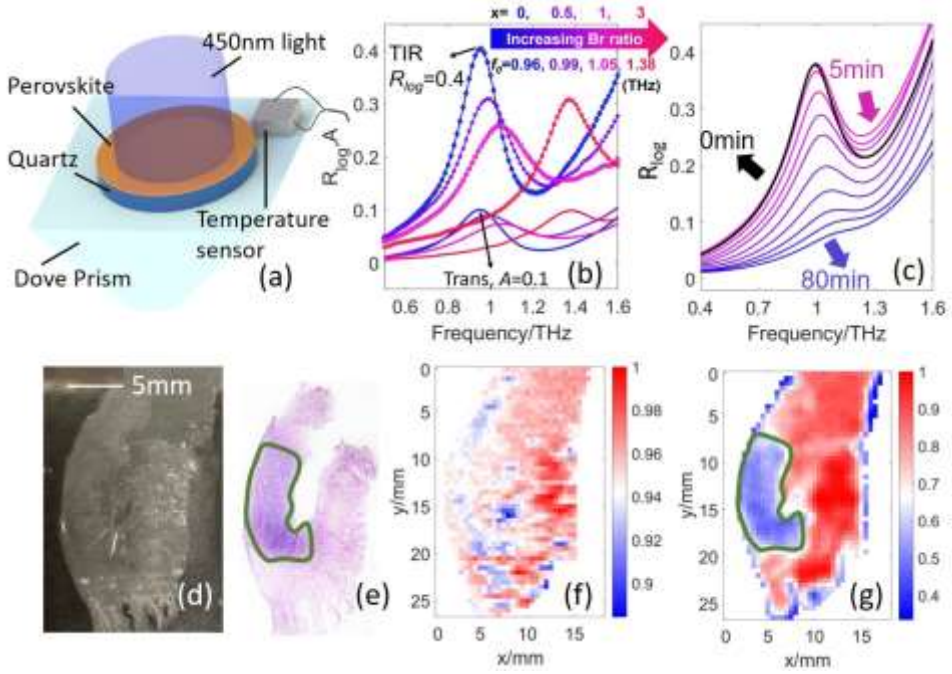

Figure 8. (a) The schematic of the TIR setup in reflection geometry. (b) Measured THz transmission and TIR spectra of $MAPbI_3$, $MAPbI_{2.5}Br_{0.5}$, $MAPbI_2Br_1$, $MAPbBr_3$. Solid lines are the results for transmission geometry, lines with the markers are the results for TIR geometry. A is the absorbance calculated from the transmission geometry, R_{log} is the logarithmic reflectance calculated from TIR, f_0 is the resonant frequency of the vibrational mode [8]. (c) THz TIR spectra of $MAPbI_{2.5}Br_{0.5}$ change under illumination, the black line indicates the spectrum before illumination. The darkest blue line indicates the spectrum after 80 min of illumination. (d) The photo of the oral cancer tissue used for THz imaging. (e) Histology image of the tissue. The cancer area is enclosed by the green line. (f) THz transmission image of the tissue at 1 THz. (g) THz multilayer reflection image of the issue a 1 THz[54].

There were two phonon modes at the low THz frequency range, "octahedral mode" (0.96 THz for $MAPbI_3$) and "Lurching mode" (2 THz for $MAPbI_3$), corresponding to X-Pb-X bond bending and stretching of the Pb-X bond coupled to MA cations in $MAPbX_3$, respectively [55]. Compared to the transmission results, the featured spectra of the perovskites were ~4 times stronger in the TIR spectra. With increasing Br ratio, the resonant frequency of the "octahedral mode" was blue-shifted, this is explained by the lower average mass at the X site when replacing I by Br ($\omega = \sqrt{k/m}$). Figure 8(c) shows the THz TIR spectra of $MAPbI_{2.5}Br_{0.5}$ under illumination. After 5 min of illumination (the black line), the strength of the "lurching mode" was increased whilst no clear change was observed in the "octahedral mode". With increasing exposure time, the intensity of the phonon modes decreased: the "octahedral mode" for this sample disappeared after 80 min of illumination. Apart from the intensity change, a blue shift in the resonant frequency of the "octahedral mode" was also observed when the perovskites were under illumination: the resonant frequencies of the phonon modes shifted from 0.96, 0.99, and 1.05 THz to around 1.11 THz for $MAPbI_3$, $MAPbI_{2.5}Br_{0.5}$, $MAPbI_2Br_1$, respectively. This was because of the formation of iodide vacancies in the perovskite films during light soaking lowering the average mass on the X site of $MAPbX_3$ and increasing the resonant frequencies of the X-Pb-X bending modes.

In conclusion, there was a two-step structural change in the perovskites under illumination, 1) the "lurching mode" was enhanced by short time illumination; and 2) both "octahedral" and "lurching"

modes were reduced by long time illumination, and the resonant frequencies of the "octahedral mode" blue-shifted. This result has provided the first experimental evidence to prove the hypothesis proposed by Gottesman et al[52] that the octahedra realign to adapt to the rotated MA cations under illumination. In short, using TIR geometry can reveal more subtle information about thin samples than transmission geometry and traditional ATR geometry. Our proposed set up is simple to implement in existing systems retrospectively and full details of the calculation approach are given in our recently published paper[8].

In addition to conductive thin films, characterization techniques for thin film liquids and low absorptive solids also need to be developed properly. In particular, characterizing thin film liquids is challenging: for example, attenuated total reflection spectroscopy[56] requires the sample thickness to be bigger than the wave penetration depth[57], making it unsuitable for thin film characterization. We have recently proposed a multilayer structure for thin film characterization in THz time domain reflection spectroscopy [54]. To realize this, the thin film liquid of interest is sandwiched between a quartz prism and a quartz substrate. The refractive index matching of the two layers surrounding the liquid enables a higher sensitivity of the characterization compared to other geometries[54]. This geometry has a higher characterization accuracy compared to the TIR regime, as the amplitude and phase information can both be used to extract the properties of the sample, whilst only the phase information is useful in TIR regime as the amplitude of the reflected signal is always 1. We have demonstrated how this multilayer structure can accurately characterize a 25 μm-thick layer of pure water, pure ethanol or the mixtures thereof[54], by only consuming a drop of the liquid. Different from metamaterial sensing, the proposed method requires neither a complicated fabrication process nor a high resolution on frequency domain, moreover, it can characterize the sample in the liquid form and

does not need to wait for it to dry out. It is potentially useful for valuable biological solution measurements and could be incorporated into a biosensing device in the future.

Apart from liquids, this multilayer structure approach is also a promising technique for enhancing contrast in THz tissue imaging. We imaged a paraffin-embedded oral cancer tissue sample using THz transmission spectroscopy and then formed the multilayer structure by sandwiching the tissue between a quartz window (bottom) and water (top) and imaged it in reflection spectroscopy[54]. Figures 8(d-e) show the photo of the sample that was used for the THz measurements and the histology image. Figures 8(f-g) give the THz transmission and multilayer reflection images, the normalized frequency-domain amplitude of the transmitted/reflected signal at 1 THz is plotted. A clear region of cancer is identified in the multilayer reflection image which matches well with the area marked out in the histology image. On the contrary, no clear boundary is observed in the transmission image. The proposed multilayer geometry improves the image contrast between the normal and cancer tissues by over a factor of 5 compared to the transmission geometry[54].

3. Single pixel THz imaging using a TIR modulator

Imaging forms the basis of many industrial and biomedical applications. However, multipixel detector arrays for THz imaging are still impeded by either high-costs or low-bandwidth. Further, most of them only provide intensity information. THz-TDS has the advantages of high temporal resolution, broad operation bandwidth and electric-field detection. These abundant attributes allow spectroscopic imaging, near-field imaging and tomography. However, the raster scanning mode for single pixel detector systems is very time-consuming which prevents it from practical applications. Thus, obtaining a method of rapid THz imaging that offers femtosecond resolution without high-costs and having high system flexibility would be ideal, and this could be achieved using “single-pixel

imaging". In this imaging modality, a set of masks is used to spatially pattern a beam of light, then by recording the transmission (or reflection) through an object for the entire mask set with a single-pixel detector, the image of the object can be reconstructed[58]. An easy way of creating a THz-spatial modulator, using commercially available equipment, is to spatially pattern a visible light beam with a digital micromirror device (DMD) and project this onto a semiconductor. This has been demonstrated in our previous work[58-59]. We found that the spatial light modulation techniques grant about ten times higher SNR for the same measurement time. However, the low modulation depth of silicon in transmission requires a high-power pumping laser. Therefore, combining this idea with the TIR geometry shown in Figure 1(a) allows for lower excitation powers and does not need a big and expensive laser system.

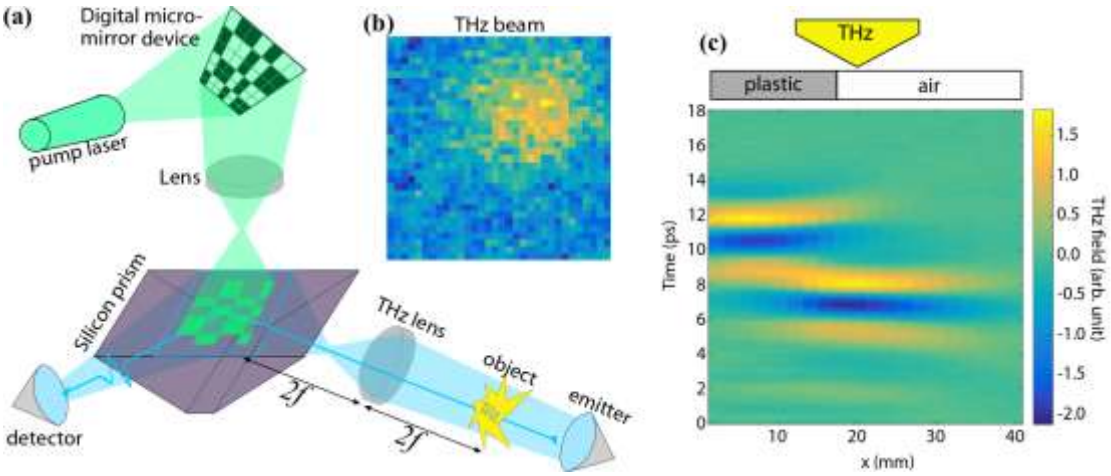

Figure 9: (a) A THz pulse is passed through an object and using a lens an image of the object is projected on the top-surface of a silicon prism. At the same time, an optical pump beam is spatially modulated and used to photoexcite the top-side of a silicon prism, which transfers the spatial encoding mask onto the THz pulse. Finally, the THz travels to a single-element detector. Knowledge of the patterns and of the corresponding detector signal are combined to give an image of the object. (b) 32x32 THz images (field of view 4x4cm) of a simple gaussian beam, where the pattern projection rate is 1kHz. (c) Hypertemporal THz 1D-line imaging. Vertical and horizontal axis are time and space respectively. Colour scale is the THz field amplitude. About half the field-of-view has plastic covering it (see above the graph).

Our imaging scheme is shown in **Figure 9(a).** We use a cheap laser diode and a DMD to project our

photoexcitation patterns in a TIR geometry, achieving greater than 90% modulation depth. The higher modulation depth allows a faster mask switching rate to be applied without losing too much SNR. Figure 9 (b) shows a 32x32 image of a Gaussian beam acquired in 1s, with a DMD switch rate of 1 kHz and 1024 masks projected. This was orders faster than our previous works which took hours[58-59]. However, the SNR of the image was relatively low because the lock-in amplifier normally applied in a THz-TDS system was removed to enable a fast switching rate. The improved acquisition rate opens the door to real-time hyperspectral THz imaging with cheap and flexible systems. In Figure 9(c), we show a hypertemporal 1D-line image where we have space (time) on the horizontal (vertical) axis and field strength on the colour scale. The object imaged was as a piece of plastic covering half of the field of view. It can be seen that the THz propagating through the plastic has taken a longer time to travel, thereby demonstrating that these systems do not sacrifice the femtosecond temporal resolution of THz-TDS systems, and frequency-domain information were are also available by applying Fourier transform to the time-domain data. Future work will focus on improving the acquisition rate even more by eliminating electrical and laser noise in the system via post-processing and better designed electronics.

4. Brewster-angle device for THz modulation

Having noted that the incident angle of THz light on the sample can significantly help or hinder its characterization, we moved from TIR to the Brewster angle. The Brewster angle refers to the incident angle at which the reflected p-polarized light is zero. The conductive thin film sensitively decreases the reflection in the TIR case while it also sensitively increases the reflection near the Brewster angle. The most obvious difference is that TIR provides very little insertion loss from the total reflection while the Brewster angle gives a deep modulation from the near zero reflection. Another benefit is

when the incident angle jumps across the Brewster angle, a 180° reverse in the phase of the reflected light occurs to reveal a large phase modulation ability. Consequently, the Brewster angle regime is also worth investigating for building functional devices. We therefore designed a graphene/quartz device operating at the Brewster angle for THz amplitude and phase modulation[18]. **Figure 10(a)** shows the schematic of the device, the graphene/Al_2O_3/TiO_x multilayer structure was deposited onto the quartz substrate, the dielectric and back gates were made of 50 nm thick Al_2O_3 and 10 nm thick TiO_x, respectively. To experimentally determine the Brewster angle, the reflections under various incident angles and different gate voltages were measured and compared to the theoretical curves calculating by using the conductivity of the graphene, with the results shown in Figure 10(b). Figure 10(c) displays the reflected time-domain signals for an incident angle of 68° when the gate voltage was 16V, 4V and -12V respectively. The change in the pulse shape from "M" to a small signal, and then to a shape of "W" indicates that the signals crossed over the Brewster angle and a broadband phase change over 140° from 0.2 THz to 1.6 THz was achieved. The device functioned as a broadband and efficient phase modulator under this incident angle.

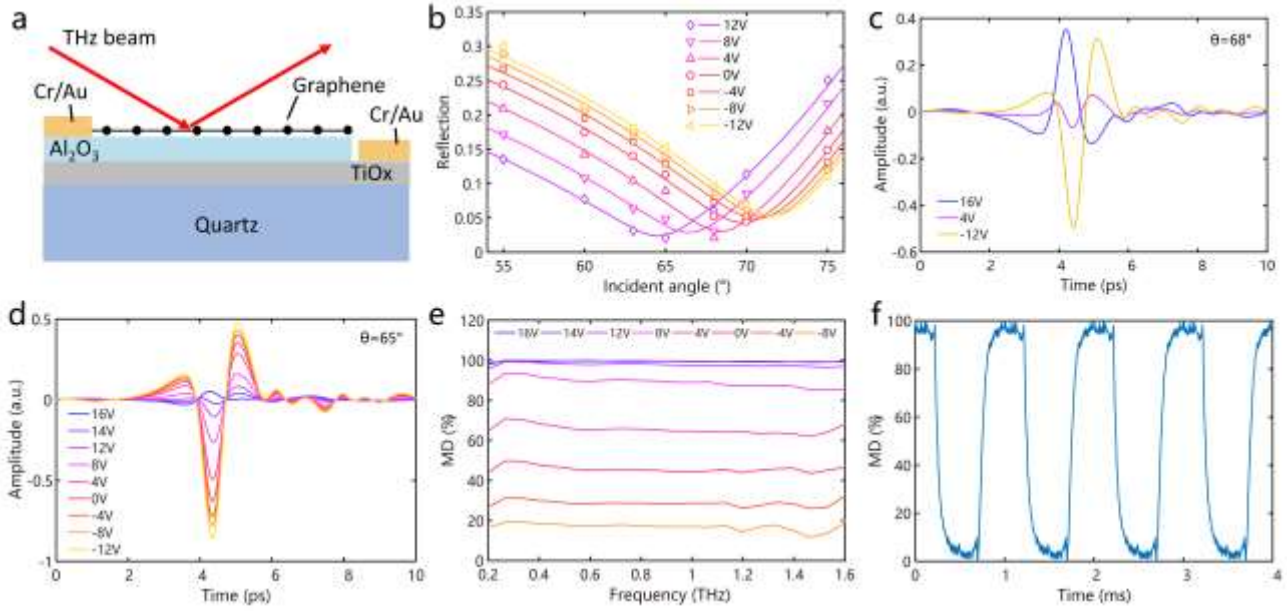

Figure 10. (a) Schematic of the graphene-quartz device. (b) Reflection as a function of incident angles Symbols are experimental data. Solid curves are theoretical calculations. (c) The time domain signals

changes with the gate voltage when incident angle being 68° and (d) 65°. (e) The corresponding modulation depth in frequency-domain when the incident angle was 65°. (f) The modulation response of the device to a 1 kHz square wave gating signal.

Consequently, this device is able to actively control the Brewster angle by varying the gate voltage rather than changing the structure of the device[18]. Figure 10(d) shows how the reflection amplitude changes under different gate voltages when the incident angle was 65°. The smallest reflection amplitude was observed when the gate voltage was 16 V as this tuned the device to be at the Brewster angle. Reducing the voltage down to -12V increased the reflection significantly as the device was shifted away from the Brewster angle. This is why deep MD can be achieved by this device. Figure 10(e) shows the corresponding modulation depths for different gate voltages in the frequency-domain. The highest MD at an incident angle of 65° was 99.9% when the gate voltage was 16 V, and the MD was higher than 99.3% in the broadband frequency range of 0.5-1.6 THz. In addition to the high MD and broadband bandwidth, this device also has a high modulation speed. As shown in Figure 10(f), under the square-wave gating signal of 1 kHz, the device can follow the modulation signal well: the rise time of the modulation was ~ 0.1 ms. The MD decreased to 60% when increasing the speed to 10 kHz. In summary, this device accomplished active control of the Brewster angle, and can modulate the THz wave with a deep MD, high modulation speed and broadband operational bandwidth significantly outperforming other modulators[18].

5. Future work

As outlined in section 3, a key goal is to create a THz imaging system that offers femtosecond temporal resolution, rapid acquisition rates and high-system flexibility without incurring great costs or adding more optical components. Adding a visible-light spatial modulator and transferring an optical pattern onto a THz beam via the photoexcitation of a semiconductor, whilst relatively simple

with existing technology, it is greatly affected by the carrier lifetimes. Longer lifetimes give increased modulation but slower switch rates, hence necessitating a trade-off between switch speed and modulation efficiency[60]. In addition, this technique is ultimately limited by the visible-light spatial modulator switch rates, currently around 20 kHz for digital micromirror devices. An electrically controlled THz spatial modulator such as a graphene array, if designed correctly, will have its switch rates limited by electronics. Furthermore, the semiconducting devices do not need the assistance of an additional pumping light, making the system more compact and flexible. From an application perspective, such a THz device is much preferred compared to transferring a visible-light pattern on a THz beam. Moreover, when imaging with such spatial modulators, the greatest reductions in noise are obtained with fully orthogonal masks (i.e. the modulated light is fully out of phase in the two masks). However, intensity-based masks that only transmit or block light have values of 1s and 0s whereas orthogonality can only be obtained with 1s and -1s. As shown in [18] when the device was working under a 68□ incident angle, we can obtain a mask with positive and negative values from a single measurement without any Lock-In subtraction detection schemes, unlike in previous work[58-59, 61]. The proposed graphene device is just as broadband and offers modulation depths close to 100% with potential switch rates in the MHz range with the correct electrical design. Of course, there are still some challenges to address from expanding the single pixel device to a modulator array, such as the manufacturing of large-scale high quality graphene, transferring it onto the substrate and connecting the layout of wires to every pixel. However, with continued advances expected in the modern semiconductor industry, the listed challenges are likely to be overcome.

Acknowledgements

This work was partially supported by the Research Grants Council of Hong Kong (project numbers

14206717 and 14201415), The Hong Kong Innovation and Technology Fund (project number ITS/371/16), the Royal Society Wolfson Merit Award (EPM) and the Hong Kong PhD Fellowship Award (QS). Authors Qiushuo Sun and Xuequan Chen, contributed equally to this work.

References

[1] S. Dhillon, M. Vitiello, E. Linfield, A. Davies, M. C. Hoffmann, J. Booske, C. Paoloni, M. Gensch, P. Weightman, G. Williams, *Journal of Physics D: Applied Physics* **2017**, 50, 043001.

[2] M. Van Exter, C. Fattinger, D. Grischkowsky, *Opt. Lett.* **1989**, 14, 1128.

[3] a) N. Katzenellenbogen, D. Grischkowsky, *Appl. Phys. Lett.* **1992**, 61, 840; b) J. Dai, J. Zhang, W. Zhang, D. Grischkowsky, *JOSA B* **2004**, 21, 1379.

[4] B. Yang, X. Wang, Y. Zhang, R. S. Donnan, *J. Appl. Phys.* **2011**, 109, 033509.

[5] P. U. Jepsen, U. Møller, H. Merbold, *Opt. Express* **2007**, 15, 14717.

[6] E. P. Parrott, J. A. Zeitler, *Appl. Spectrosc.* **2015**, 69, 1.

[7] Q. Sun, Y. He, K. Liu, S. Fan, E. P. Parrott, E. Pickwell-MacPherson, *Quantitative imaging in medicine and surgery* **2017**, 7, 345.

[8] Q. Sun, X. Liu, J. Cao, R. I. Stantchev, Y. Zhou, X. Chen, E. P. Parrott, J. Lloyd-Hughes, N. Zhao, E. Pickwell-MacPherson, *J. Phys. Chem. C* **2018**, 122, 17552.

[9] Q. Sun, E. P. Parrott, Y. He, E. Pickwell-MacPherson, *Journal of biophotonics* **2018**, 11, e201700111.

[10] a) D. H. Auston, *Appl. Phys. Lett.* **1975**, 26, 101; b) B. Sartorius, H. Roehle, H. Künzel, J. Böttcher, M. Schlak, D. Stanze, H. Venghaus, M. Schell, *Opt. Express* **2008**, 16, 9565.

[11] a) A. Bonvalet, M. Joffre, J. Martin, A. Migus, *Appl. Phys. Lett.* **1995**, 67, 2907; b) L.-L. Zhang, W.-M. Wang, T. Wu, R. Zhang, S.-J. Zhang, C.-L. Zhang, Y. Zhang, Z.-M. Sheng, X.-C. Zhang, *Phys. Rev. Lett.* **2017**, 119, 235001.

[12] B. Ferguson, X.-C. Zhang, *Nat. Mater.* **2002**, 1, 26.

[13] a) A. Dobroiu, M. Yamashita, Y. N. Ohshima, Y. Morita, C. Otani, K. Kawase, *Appl. Opt.* **2004**, 43, 5637; b) P. Kühne, N. Armakavicius, V. Stanishev, C. M. Herzinger, M. Schubert, V. Darakchieva, *IEEE Transactions on Terahertz Science and Technology* **2018**, 8, 257.

[14] a) P. F.-X. Neumaier, H. Richter, J. Stake, H. Zhao, A.-Y. Tang, V. Drakinskiy, P. Sobis, A. Emrich, A. Hülsmann, T. K. Johansen, *IEEE transactions on terahertz science and technology* **2014**, 4, 469; b) N. Karpowicz, J. Dai, X. Lu, Y. Chen, M. Yamaguchi, H. Zhao, X.-C. Zhang, L. Zhang, C. Zhang, M. Price-Gallagher, *Appl. Phys. Lett.* **2008**, 92, 011131.

[15] T. Bryllert, J. Svedin, M. Karlsson, E. Gandini, N. Llombart, V. Drakinskiy, J. Stake, presented at Society of Photo-Optical Instrumentation Engineers (SPIE) Conference Series **2018**.

[16] a) A. A. Generalov, M. A. Andersson, X. Yang, A. Vorobiev, J. Stake, *IEEE Transactions on Terahertz Science and Technology* **2017**, 7, 614; b) A. Lisauskas, M. Bauer, S. Boppel, M. Mundt, B. Khamaisi, E. Socher, R. Venckevičius, L. Minkevičius, I. Kašalynas, D. Seliuta, *Journal of Infrared, Millimeter, and Terahertz Waves* **2014**, 35, 63; c) V. Popov, D. Ermolaev, K. Maremyanin, N. Maleev, V. Zemlyakov, V. Gavrilenko, S. Y. Shapoval, *Appl. Phys. Lett.* **2011**, 98, 153504.

[17] a) X. Liu, E. P. Parrott, B. S.-Y. Ung, E. Pickwell-MacPherson, *APL Photonics* **2016**, 1, 076103; b) X. Liu, Z. Chen, E. P. Parrott, B. S. Y. Ung, J. Xu, E. Pickwell-MacPherson, *Adv. Opt. Mater.* **2017**, 5.

[18] Z. Chen, X. Chen, L. Tao, K. Chen, M. Long, X. Liu, K. Yan, R. I. Stantchev, E. Pickwell-MacPherson, J.-B. Xu, *Nature communications* **2018**, 9.

[19] M. Rahm, J.-S. Li, W. J. Padilla, *Journal of Infrared, Millimeter, and Terahertz Waves* **2013**, 34, 1.

[20] T. Matsui, H. Mori, Y. Inose, S. Kuromiya, K. Takano, M. Nakajima, M. Hangyo, *Jpn. J. Appl. Phys.* **2016**, 55, 03DC12.

[21] Y. Cao, S. Gan, Z. Geng, J. Liu, Y. Yang, Q. Bao, H. Chen, *Sci. Rep.* **2016**, 6, 22899.

[22] C.-Y. XIA, Z. Fang, Y. Huang, B. Wang, Z. Li, L. Wang, X. Wu, presented at International Symposium on Ultrafast Phenomena and Terahertz Waves **2018**.

[23] J. Yuan, W. Jiang, W. Xu, J. Yang, S. Gong, S. Imran, L. Xie, Y. Ying, Y. Ma, *Optical Materials Express* **2016**, 6, 3908.

[24] N. Kakenov, T. Takan, V. A. Ozkan, O. Balcı, E. O. Polat, H. Altan, C. Kocabas, *Opt. Lett.* **2015**, 40, 1984.

[25] J. Han, A. Lakhtakia, *Journal of Modern Optics* **2009**, 56, 554.

[26] M. Shalaby, M. Peccianti, Y. Ozturk, I. Al-Naib, C. P. Hauri, R. Morandotti, *Appl. Phys. Lett.* **2014**, 105, 151108.

[27] D. Huang, E. Poutrina, D. R. Smith, *Appl. Phys. Lett.* **2010**, 96, 104104.

[28] A. Thoman, A. Kern, H. Helm, M. Walther, *Physical Review B* **2008**, 77, 195405.

[29] a) S. McKnight, K. Stewart, H. Drew, K. Moorjani, *Infrared physics* **1987**, 27, 327; b) J. Kröll, J. Darmo, K. Unterrainer, *Opt. Express* **2007**, 15, 6552; c) Y. Zhou, X. Xu, F. Hu, X. Zheng, W. Li, P. Zhao, J. Bai, Z. Ren, *Appl. Phys. Lett.* **2014**, 104, 051106.

[30] R. Wang, X.-G. Ren, Z. Yan, L.-J. Jiang, E. Wei, G.-C. Shan, *Frontiers of Physics* **2019**, 14, 13603.

[31] Y. Harada, M. S. Ukhtary, M. Wang, S. K. Srinivasan, E. H. Hasdeo, A. R. Nugraha, G. T. Noe, Y. Sakai, R. Vajtai, P. M. Ajayan, *ACS Photonics* **2016**.

[32] a) Z. Miao, Q. Wu, X. Li, Q. He, K. Ding, Z. An, Y. Zhang, L. Zhou, *Physical Review X* **2015**, 5, 041027; b) Y. Wu, C. La-o-vorakiat, X. Qiu, J. Liu, P. Deorani, K. Banerjee, J. Son, Y. Chen, E. E. Chia, H. Yang, *Adv. Mater.* **2015**, 27, 1874.

[33] A. Novitsky, A. M. Ivinskaya, M. Zalkovskij, R. Malureanu, P. U. Jepsen, A. V. Lavrinenko, *Journal of Applied Physics* **2012**, 112, 074318.

[34] S.-F. Shi, B. Zeng, H.-L. Han, X. Hong, H.-Z. Tsai, H. Jung, A. Zettl, M. Crommie, F. Wang, *Nano Lett.*

2014, 15, 372.

[35] Y. Sun, R. Degl'Innocenti, D. A. Ritchie, H. E. Beere, L. Xiao, M. Ruggiero, J. A. Zeitler, R. I. Stantchev, D. Chen, Z. Peng, *Photonics Research* **2018**, 6, 1151.

[36] a) F. Yan, C. Yu, H. Park, E. P. Parrott, E. Pickwell-MacPherson, *Journal of infrared, millimeter, and terahertz waves* **2013**, 34, 489; b) Z. Huang, H. Park, E. P. Parrott, H. P. Chan, E. Pickwell-MacPherson, *IEEE Photonics Technology Letters* **2013**, 25, 81; c) A. Partanen, J. Väyrynen, S. Hassinen, H. Tuovinen, J. Mutanen, T. Itkonen, P. Silfsten, P. Pääkkönen, M. Kuittinen, K. Mönkkönen, *Appl. Opt.* **2012**, 51, 8360; d) A. Ferraro, D. Zografopoulos, M. Missori, M. Peccianti, R. Caputo, R. Beccherelli, *Opt. Lett.* **2016**, 41, 2009; e) L. Deng, J. Teng, L. Zhang, Q. Wu, H. Liu, X. Zhang, S. Chua, *Appl. Phys. Lett.* **2012**, 101, 011101; f) Z. Huang, E. P. Parrott, H. Park, H. P. Chan, E. Pickwell-MacPherson, *Opt. Lett.* **2014**, 39, 793; g) I. Yamada, K. Takano, M. Hangyo, M. Saito, W. Watanabe, *Opt. Lett.* **2009**, 34, 274.

[37] a) C.-S. Yang, T.-T. Tang, P.-H. Chen, R.-P. Pan, P. Yu, C.-L. Pan, *Opt. Lett.* **2014**, 39, 2511; b) H.-Y. Wu, C.-F. Hsieh, T.-T. Tang, R.-P. Pan, C.-L. Pan, *IEEE Photonics Technology Letters* **2006**, 18, 1488; c) L. Wang, X.-W. Lin, W. Hu, G.-H. Shao, P. Chen, L.-J. Liang, B.-B. Jin, P.-H. Wu, H. Qian, Y.-N. Lu, *Light: Science & Applications* **2015**, 4, e253.

[38] a) B. Vasić, D. C. Zografopoulos, G. Isić, R. Beccherelli, R. Gajić, *Nanotechnology* **2017**, 28, 124002; b) X. Liu, X. Chen, E. P. Parrott, E. Pickwell-MacPherson, *Photonics Research* **2017**, 5, 299; c) L. Cong, N. Xu, J. Gu, R. Singh, J. Han, W. Zhang, *Laser & Photonics Reviews* **2014**, 8, 626; d) N. K. Grady, J. E. Heyes, D. R. Chowdhury, Y. Zeng, M. T. Reiten, A. K. Azad, A. J. Taylor, D. A. Dalvit, H.-T. Chen, *Science* **2013**, 340, 1304; e) C. Han, E. P. Parrott, E. Pickwell-MacPherson, *IEEE Journal of Selected Topics in Quantum Electronics* **2017**, 23, 1; f) X. Liu, X. Chen, E. P. Parrott, C. Han, G. Humbert, A. Crunteanu, E. Pickwell-MacPherson, *APL Photonics* **2018**, 3, 051604.

[39] C.-Y. Chen, C.-F. Hsieh, Y.-F. Lin, R.-P. Pan, C.-L. Pan, *Opt. Express* **2004**, 12, 2625.

[40] a) D. Wang, L. Zhang, Y. Gu, M. Mehmood, Y. Gong, A. Srivastava, L. Jian, T. Venkatesan, C.-W. Qiu, M. Hong, *Sci. Rep.* **2015**, 5, 15020; b) L. Cong, Y. K. Srivastava, H. Zhang, X. Zhang, J. Han, R. Singh, *Light: Science & Applications* **2018**, 7, 28; c) Q. Wang, E. Plum, Q. Yang, X. Zhang, Q. Xu, Y. Xu, J. Han, W. Zhang, *Light: Science & Applications* **2018**, 7, 25.

[41] X. Chen, R. I. Stantchev, E. Pickwell-MacPherson, Employing metallic grating in total internal reflection geometry for polarization control, https://1drv.ms/v/s!AnRiwaTXTTkJiQyMLJOidyk4aYEE, accessed.

[42] H.-F. Zhu, L.-H. Du, J. Li, Q.-W. Shi, B. Peng, Z.-R. Li, W.-X. Huang, L.-G. Zhu, *Appl. Phys. Lett.* **2018**, 112, 081103.

[43] X. Chen, E. P. Parrott, B. S.-Y. Ung, E. Pickwell-MacPherson, *IEEE Transactions on Terahertz Science and Technology* **2017**, 7, 493.

[44] P. U. Jepsen, D. G. Cooke, M. Koch, *Laser & Photonics Reviews* **2011**, 5, 124.

[45] X. Chen, E. P. Parrott, Z. Huang, H.-P. Chan, E. Pickwell-MacPherson, *Photonics Research* **2018**, 6, 768.

[46] S. Knight, D. Prabhakaran, C. Binek, M. Schubert, *Sci. Rep.* **2019**, 9, 1353.

[47] a) S. Knight, S. Schöche, V. Darakchieva, P. Kühne, J.-F. Carlin, N. Grandjean, C. Herzinger, M. Schubert, T. Hofmann, *Opt. Lett.* **2015**, 40, 2688; b) T. Hofmann, P. Kühne, S. Schöche, J.-T. Chen, U. Forsberg, E. Janzén, N. Ben Sedrine, C. Herzinger, J. A. Woollam, M. Schubert, *Appl. Phys. Lett.* **2012**, 101, 192102.

[48] J.-P. Correa-Baena, M. Saliba, T. Buonassisi, M. Grätzel, A. Abate, W. Tress, A. Hagfeldt, *Science* **2017**, 358, 739.

[49] Z. Xiao, R. A. Kerner, L. Zhao, N. L. Tran, K. M. Lee, T.-W. Koh, G. D. Scholes, B. P. Rand, *Nat. Photonics* **2017**, 11, 108.

[50] H. Zhu, Y. Fu, F. Meng, X. Wu, Z. Gong, Q. Ding, M. V. Gustafsson, M. T. Trinh, S. Jin, X. Zhu, *Nat. Mater.* **2015**, 14, 636.

[51] G. Niu, X. Guo, L. Wang, *J. Mater. Chem. A* **2015**, 3, 8970.

[52] R. Gottesman, L. Gouda, B. S. Kalanoor, E. Haltzi, S. Tirosh, E. Rosh-Hodesh, Y. Tischler, A. Zaban, C. Quarti, E. Mosconi, *J. Phys. Chem. Lett.* **2015**, 6, 2332.

[53] R. L. Milot, G. E. Eperon, H. J. Snaith, M. B. Johnston, L. M. Herz, *Adv. Funct. Mater.* **2015**, 25, 6218.

[54] Q. Sun, K. Liu, X. Chen, X. Liu, A. Hernandez-Serrano, E. Pickwell-MacPherson, *Opt. Lett.* **Accepted, 2019**.

[55] A. M. Leguy, A. R. Goñi, J. M. Frost, J. Skelton, F. Brivio, X. Rodríguez-Martínez, O. J. Weber, A. Pallipurath, M. I. Alonso, M. Campoy-Quiles, *PCCP* **2016**, 18, 27051.

[56] H. Hirori, K. Yamashita, M. Nagai, K. Tanaka, *Jpn. J. Appl. Phys.* **2004**, 43, L1287.

[57] G. Laroche, J. Fitremann, N. Gherardi, *Appl. Surf. Sci.* **2013**, 273, 632.

[58] R. I. Stantchev, B. Sun, S. M. Hornett, P. A. Hobson, G. M. Gibson, M. J. Padgett, E. Hendry, *Science advances* **2016**, 2, e1600190.

[59] R. I. Stantchev, D. B. Phillips, P. Hobson, S. M. Hornett, M. J. Padgett, E. Hendry, *Optica* **2017**, 4, 989.

[60] A. Kannegulla, M. I. B. Shams, L. Liu, L.-J. Cheng, *Opt. Express* **2015**, 23, 32098.

[61] C. M. Watts, D. Shrekenhamer, J. Montoya, G. Lipworth, J. Hunt, T. Sleasman, S. Krishna, D. R. Smith, W. J. Padilla, *Nat. Photonics* **2014**, 8, 605.

List of Figures

Linear-circular polarization switch by the proposed TIR-VO_2-grating device. p-polarized linear output when the VO_2 was at the insulating phase. (c) Circular polarization output when the VO_2 was at the metallic phase. (d) Diagram of the same TIR-VO_2-grating device coupled with a quartz prism. (e) Modulation depth as a function of frequency. The white area shows the effective region and the gray area has a low SNR.

Figure 8. (a) The schematic of the TIR setup in reflection geometry. (b) Measured THz transmission and TIR spectra of $MAPbI_3$, $MAPbI_{2.5}Br_{0.5}$, $MAPbI_2Br_1$, $MAPbBr_3$. Solid lines are the results for transmission geometry, lines with the markers are the results for TIR geometry. A is the absorbance calculated from the transmission geometry, R_{log} is the logarithmic reflectance calculated from TIR, f_0 is the resonant frequency of the vibrational mode [8]. (c) THz TIR spectra of $MAPbI_{2.5}Br_{0.5}$ change under illumination, the black line indicates the spectrum before illumination. The darkest blue line indicates the spectrum after 80 min of illumination. (d) The photo of the oral cancer tissue used for THz imaging. (e) Histology image of the tissue. The cancer area is enclosed by the green line. (f) THz transmission image of the tissue at 1 THz. (g) THz multilayer reflection image of the issue a 1 THz[54].

Figure 9: (a) A THz pulse is passed through an object and using a lens an image of the object is projected on the top-surface of a silicon prism. At the same time, an optical pump beam is spatially modulated and used to photoexcite the top-side of a silicon prism, which transfers the spatial encoding mask onto the THz pulse. Finally, the THz travels to a single-element detector. Knowledge of the patterns and of the corresponding detector signal are combined to give an image of the object. (b) 32x32 THz images (field of view 4x4cm) of a simple gaussian beam, where the pattern projection rate is 1kHz. (c) Hypertemporal THz 1D-line imaging. Vertical and horizontal axis are time and space respectively. Colourscale is the THz field amplitude. About half the field-of-view has plastic covering it (see above the graph).

Figure 10. (a) Schematic of the graphene-quartz device. (b) Reflection as a function of incident angles Symbols are experimental data. Solid curves are theoretical calculations. (c) The time domain signals changes with the gate voltage when incident angle being 68° and (d) 65°. (e) The corresponding modulation depth in frequency-domain when the incident angle was 65°. (f) The modulation response of the device to a 1 KHz square wave gating signal.

Qiushuo Sun is currently a PhD Candidate in the Department of Electronic Engineering at the Chinese University of Hong Kong. She received the B. Eng. degree in communication engineering from Northeastern University (China), in 2015. Her research interests include terahertz spectroscopy, terahertz material characterization and biomedical imaging.

Dr. Xuequan Chen received the B.Eng. degree (Honors) from University of Electronic Science and Technology of China in 2014. After that, he joined Prof. Emma Pickwell-MacPherson's Terahertz group in the Chinese University of Hong Kong for his PhD research and completed his PhD degree in 2018. He is now a postdoctoral fellow and continues his research in fast and accurate terahertz spectroscopy and imaging, ellipsometry and advanced terahertz devices.

Emma Pickwell-MacPherson studied Natural Sciences for her undergraduate degree at Cambridge University followed by an MSci in Physics where she specialized in semiconductor physics. She completed her PhD in 2005 with the Semiconductor Physics Group at Cambridge University, sponsored by TeraView Ltd. Her PhD work focused on understanding contrast mechanisms in terahertz images of skin cancer. More recently her research has encompassed developing THz devices, instrumentation and algorithms to improve THz metrology, ultimately with a view to applying THz imaging to biomedical applications.